Azide-rich complexes of cobalt(III) with the rare 5-phenyl-2,2'-bipyridine ligand

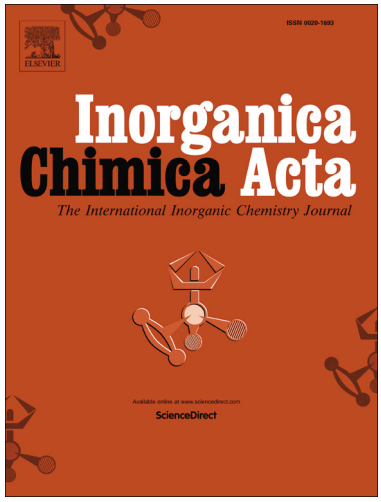

Research paper

Azide-rich complexes of cobalt(III) with the rare 5-phenyl-2,2'-bipyridine ligand

Damir A. Safin, Koen Robeyns, Christophe M.L. Vande Velde, Mike Thijs, Mariusz P. Mitoraj, Filip Sagan, Yaroslav Filinchuk

PII: S0020-1693(16)30789-7
DOI: http://dx.doi.org/10.1016/j.ica.2017.01.020
Reference: ICA 17413

To appear in: *Inorganica Chimica Acta*

Received Date: 30 October 2016
Revised Date: 21 December 2016
Accepted Date: 27 January 2017

Please cite this article as: D.A. Safin, K. Robeyns, C.M.L. Vande Velde, M. Thijs, M.P. Mitoraj, F. Sagan, Y. Filinchuk, Azide-rich complexes of cobalt(III) with the rare 5-phenyl-2,2'-bipyridine ligand, *Inorganica Chimica Acta* (2017), doi: http://dx.doi.org/10.1016/j.ica.2017.01.020

Azide-rich complexes of cobalt(III) with the rare 5-phenyl-2,2'-bipyridine ligand

Damir A. Safin *[,a], Koen Robeyns [a], Christophe M. L. Vande Velde [b], Mike Thijs [b], Mariusz P. Mitoraj *[,c], Filip Sagan [c], Yaroslav Filinchuk [a]

[a] *Institute of Condensed Matter and Nanosciences, Molecules, Solids and Reactivity (IMCN/MOST), Université catholique de Louvain, Place L. Pasteur 1, 1348 Louvain-la-Neuve, Belgium*

[b] *Faculty of Applied Engineering, Advanced Reactor Technology, University of Antwerp, Groenenborgerlaan 171, 2018 Antwerpen, Belgium*

[c] *Department of Theoretical Chemistry, Faculty of Chemistry, Jagiellonian University, R. Ingardena 3, 30-060 Cracow, Poland*

Abstract Reaction of one or two equivalents of 5-phenyl-2,2'-bipyridine (**L**) with a mixture of one equivalent of $CoCl_2$ and two equivalents of NaN_3 leads to mononuclear heteroleptic cobalt(III) complexes $[CoL_2(N_3)_2](N_3)_{0.55}Cl_{0.45}\cdot EtOH$ (**1**) and $[CoL_2(N_3)_2]N_3\cdot 2.5EtOH$ (**2**), respectively. Both structures reveal that cobalt(III) atom is linked to the six nitrogen atoms of two **L** and two N_3^- anions. Both structures are stabilized by intermolecular C–H···N and $\pi\cdots\pi$ stacking interactions. TG and DSC analyses reveal **1** being stable up to 63 °C and decomposing in three steps, **2** on the other hand decomposes at 84 °C in two steps. Both decomposition pathways start with an endothermic loss of the lattice ethanol molecules. The second step in **1** (177 °C) and **2** (196 °C) is related to the "jet" effect, seen as an abrupt weight loss due to a drastic energy release upon heating. In **2** this is the result of a release of N_2 gas from the azides and decomposition of the ligands **L** followed by the full reduction of cobalt(III) to cobalt(0). In **1** there is a loss of one azide accompanied by the reduction of cobalt(III) to cobalt(II). The final decomposition step of **1** at 215 °C is attributed to the exothermic decomposition of **L** and remaining azide with the formation of a mixture of

* Corresponding author.
E-mail address: damir.a.safin@gmail.com (D. A. Safin), mitoraj@chemia.uj.edu.pl (M. P. Mitoraj).

$CoCl_2$ and Co_2N. DFT calculations are performed in order to shed additional light on possible spin states of cobalt complexes as well as to rationalize the stability of the synthesized materials.

Keywords: Cobalt; Azide; X-ray crystallography; Thermal analysis; DFT

1. Introduction

Azide (N_3^-) is an important constituent of the compounds that play a pivotal role as propellants in air bags [1]. In particular, lead and copper azides are of importance as explosives [2,3]. Intuitively, a better energy source may be achieved through enrichment of the azide content in a metal complex. As such, thermal decomposition of the metal azide seems to be a powerful tool in the design and fabrication of materials for the controlled release of thermal energy. This can be achieved by varying not only the azide content but also its binding mode. Particularly, the azide anion is known to bind metal ions in a number of bonding modes varying from terminal, end-on bridging to end-to-end bridging modes or ionic. The binding mode of the azide ligand, obviously, depends on the nature and the oxidation state of a central metal ion, as well as the nature of other coordinated ligands. An additional role of the latter is to uphold the different stability of the metal azide.

Cobalt forms stable azide complexes [4–6] and has different stable oxidation states. This makes cobalt azide complexes promising materials for tunable heat energy release during their thermal degradation. Even more telling is that the first ever structurally characterized metal azide was the azidopentamminecobalt(III) azide, $[Co(NH_3)_5(N_3)](N_3)_2$ [7].

On the other hand *N*-heterocyclic ligands, in particular polypyridine compounds, serve as multidentate ligands that give characteristic properties to the metal complexes that they form. These ligands can be easily modified by introducing different substituents, imposing a variety of electronic, steric and conformational effects on both the coordinated chelate and coordination core. *N*-heterocyclic compounds such as 2,2'-bipyridine, 1,10-phenanthroline and 2,2':6',2''-terpyridine seem to be the most widely used polypyridine ligands for metal complexes as well as building units in coordination and supramolecular chemistry. In particular, these compounds are known to be efficient ligands for dye-sensitized solar cells [8]. Furthermore,

the renaissance of a highly attractive ligand, owing to the presence of three fused terpyridine-like coordination pockets, 2,4,6-tris(2-pyrimidyl)-1,3,5-triazine has recently been announced [9]. Although 2,4,6-tris(2-pyrimidyl)-1,3,5-triazine has been known for almost 60 years [10], its coordination chemistry remains vastly underexplored. Indeed, until recently only two coordination compounds of 2,4,6-tris(2-pyrimidyl)-1,3,5-triazine were known in the literature [11,12]. However, during the last two years the number of reported complexes built from 2,4,6-tris(2-pyrimidyl)-1,3,5-triazine has quadrupled [13–19].

With this in mind, we have recently directed our attention to the 5-phenyl-2,2'-bipyridine (**L**), which was synthesized according to a known procedure [20,21]. It was established, that the reaction of **L** with a mixture of CuHal (Hal = Cl^-, Br^-, I^-) or $[Cu(CH_3CN)_4]BF_4$ and PPh_3 leads to the mononuclear heteroleptic complexes $[CuL(PPh_3)Hal]$ and $[CuL(PPh_3)_2]BF_4$, respectively [22,23]. All compounds were found to be emissive in the solid state. DFT calculations have shown that, while emission of **L** is due to the ligand-centered $\pi \rightarrow \pi^*$ transition, luminescence of $[CuL(PPh_3)Hal]$ and $[CuL(PPh_3)_2]BF_4$ is attributed to (M + Hal)LCT and MLCT excited states, respectively. We have also described the synthesis and complete structural investigation of Ag^I complexes of **L**, namely $[AgL_2]NO_3{\cdot}0.5H_2O$ and $[AgLPPh_3NO_3]{\cdot}0.5CH_2Cl_2$, which were obtained through the direct reaction of **L** with $AgNO_3$ or with a mixture of $AgNO_3$ and PPh_3, respectively [24]. Furthermore, conversion of the first complex into the second one upon reacting with PPh_3 was also described.

In this contribution, we continue our comprehensive research of the complexation properties of **L**. We describe the synthesis and complete structural investigation of the mononuclear heteroleptic cobalt(III) complexes $[CoL_2(N_3)_2](N_3)_{0.55}Cl_{0.45}{\cdot}EtOH$ (**1**) and $[CoL_2(N_3)_2]N_3{\cdot}2.5EtOH$ (**2**) as well as their thermal decomposition.

2. Results and discussion

The complexes **1** and **2** were prepared by reacting $CoCl_2$ with two equivalents of NaN_3, followed by the addition of one or two equivalents of **L**, respectively, in an ethanol/acetonitrile mixture under ambient conditions (Scheme 1). The obtained red crystals are soluble in most polar solvents. It should be noted, that the composition of **2** was suggested based on the elemental analysis data, which best fit corresponds to the

presence of about two and a half molecules of ethanol per one $[CoL_2(N_3)_2]N_3$ species. This finding is further supported by the ^{1}H NMR spectroscopy and TGA data (see below) as well as by the presence of cavities with non-discrete solvent molecules account for the 69 electrons as evidenced from single crystal X-ray diffraction.

Our initial goal was the synthesis of heteroleptic azide-containing cobalt(II) complexes with **L** yielding new hybrid materials displaying interesting magnetic properties such as single-molecule and single-chain magnet behaviour. With respect to this, it was supposed that using two equivalents of **L** most likely lead to the formation of a discrete cobalt(II) complex **$[CoL_2(N_3)_2]$**, exhibiting an octahedral coordination mode, while adding of one equivalent of **L** to a reaction mixture should support the formation of a polymeric cobalt(II) 1D chain structure **$[CoL(N_3)_2]_n$**, constructed also from coordination octahedra (Chart 1). Both synthetic strategies may also afford a tetrahedral cobalt(II) structure (Chart 1). It was, however, found that both synthetic strategies yields mononuclear heteroleptic salt-like complexes of cobalt(III), each containing the same $[CoL_2(N_3)_2]^+$·cation, where the metal center is octahedrally coordinated (Scheme 1). Thus, the cobalt(II) cation is further oxidized to cobalt(III) under the synthetic conditions. This might be explained by the coordination of two ligands **L** with the subsequent oxidation of the metal center similar to that of the formation of the hexamminecobalt(III) salts upon reacting cobalt(II) salts with NH_3 [25].

The ^{1}H NMR spectra of **1** and **2** in DMSO-d_6 are the same and each exhibit a triplet at about 8.00 ppm and three multiplets at 7.37–7.65, 8.28–8.44 and 8.68–8.84 ppm corresponding to the ligands **L**. Besides all, the spectra contain characteristic signals for the ethanol molecules: a triplet at about 1.10 ppm and a quartet at about 3.40 ppm with coupling constants $^3J_{H,H}$ = 7.0 Hz. The relative ratio of integral intensities of the signals of **L** and ethanol supports the presence of one and about two and a half molecules of ethanol per two ligands **L** in **1** and **2**, respectively. It should be noted that the spectra exhibit signals exclusively in the diamagnetic region (0–14 ppm), testifying to the presence of low spin diamagnetic cobalt(III) species.

The coordination chemistry of DMSO to transition metals has been thoroughly studied [26]. DMSO can exhibit *S*-, *O*-, or bridging μ-*S*,*O*-bound coordination modes. In the ^{1}H NMR spectra, *O*- and *S*-bound DMSO ligands exhibit ^{1}H NMR chemical shifts at 2.60–3.05 and 3.30–3.80 ppm, respectively [27]. In the ^{1}H NMR spectra of both **1** and **2**, the solvent signal was exclusively observed at 2.50 ppm testifying to the

presence of free DMSO. Furthermore, all the signals of **L** and DMSO in the ^{1}H NMR spectra of the complexes were shown as narrow signals testifying to the absence of exchange between these species, at least under experimental conditions.

According to the X-ray data, **1** and **2** each crystallize in the triclinic space group *P*–1, and both exhibit an ionic structure comprising a discrete cation $[CoL_2(N_3)_2]^+$·and a N_3^- anion (Fig. 1). In the structure of **1**, the non-bound azide anion is found in combination with Cl^- with a ratio of about 55% to 45% in a favour of the former anion. The asymmetric unit of **1** also contains one molecule of ethanol, which is disordered over two positions with a 73% and 27% ratio. The asymmetric unit of **2** contains two independent $[CoL_2(N_3)_2]N_3$ molecules, namely **2-I** and **2-II**. Notably, **2** contains two cavities of 194 Å^3 with non-discrete solvent molecules accounting for 69 electrons each. The latter is in good agreement with two and a half ethanol molecules (65 electrons) found from the elemental analysis and ^{1}H NMR spectroscopy data. In both structures the cobalt(III) atom is linked to the nitrogen atoms of two **L** and two *cis*-coordinated N_3^- with the formation of a distorted octahedral coordination core. This distortion is due to the small bite angle of **L** (Table 1). The two pyridine moieties of **L** are almost in the same plane for both complexes, which is reflected in the dihedral angles ranging from 2.2(14)° to 7.33(18)° between the two cycles (Fig. 2, Table 1). However, the phenyl fragments deviate significantly from the pyridine planes for both structures with the most significant deviation observed for both ligands **L** in the structure of **1** (Fig. 2, Table 1).

Notably, a comprehensive study of the Cambridge Structural Database (CSD) revealed only 92 hits for metal complexes containing ionic azide species, and only a handful of these hits (9) correspond to cobalt complexes [28,29]. Thus, the crystal structures of both **1** and **2** belong to an extremely rare family of cobalt-based complexes with non-bound azide anions.

The Co–N(Py) bond lengths in **1**, **2-I** and **2-II** are very similar and range from 1.93 Å to 1.98 Å (Table 1). The Co–N_3 bond lengths are almost identical in the structure of **1** and about 1.94 Å, while the same bonds differ significantly in the structures of both molecules of **2**. In particular, while one of the Co–N_3 bonds is of 1.89–1.91 Å, the second Co–N_3 bond is significantly longer and of about 1.98–2.04 Å (Table 1). The chelate N(Py)–Co–N(Py) bond angles are about 82.0° in all the **1**, **2-I** and **2-II** molecules, while the exocyclic N(Py)–Co–N(Py) bond angles vary from 88.0° to 97.5° and from 175.0° to 177.4° (Table 1). The N(Py)–

Co–N_3 bond angles in the structures of **1** and **2-II** fit almost the same ranges and of about 84.8–92.4° and 171.0–174.5°, while the same angles in the structure of **2-I** deviates significantly and of about 79.7–92.1° and 167.5–173.8° (Table 1). The N_3–Co–N_3 bond angle increases from 91.95(13)° to 98.7(12)° to 102.6(12)° for **1**, **2-II** and **2-I**, respectively.

Notably, the structures of **1** and **2** are each stabilised by a network of intermolecular C–H···N interactions, formed by the hydrogen atoms of the ligands **L** and nitrogen atoms of both the coordinated and ionic azide anions (Table 2). The structure of **1** also contains intermolecular C–H···Cl interactions (Table 2). Both structures **1** and **2** are additionally stabilized by weak intermolecular parallel displaced $\pi\cdots\pi$ stacking interactions (Table 3). While these interactions in the structure of **1** are formed between the terminal pyridine fragments of the two isotype ligands **L** corresponding to two adjacent cations, the same interactions in the structure of **2** are formed between the terminal pyridine and phenyl fragments of the two isotype ligands **L** corresponding to two adjacent cations of **2-I** and **2-II** (Table 3).

The $[CoL_2(N_3)_2]^+$·cations in the structure of **1** are packed into double layered 2D sheets along the *ab* plane (Fig. 3). These 2D sheets are further interlinked through the above-mentioned $\pi\cdots\pi$ stacking interactions (Table 3) with the formation of 1D channels propagated along the *b* axis. These channels are filled by ionic N_3^-, Cl^- and lattice ethanol molecules (Fig. 3). Cations in the structure of **2** are also packed into double-layered 2D sheets along the *ab* plane (Fig. 3), equally stabilized through the above-mentioned $\pi\cdots\pi$ stacking interactions (Table 3) between the molecules arising from both layers. Furthermore, these 2D sheets are separated from each other by a single layered 2D sheet of ionic N_3^- anions, which, in turn, are oriented along the *a* axis (Fig. 3).

The thermal properties of **1** and **2** were studied by means of TG and DSC analyses. The molecules of **1** and **2** are stable up to 63 and 84 °C, and decompose in three and two clearly defined steps, respectively (Fig. 4). The first step for both complexes corresponds to the *endo*thermic loss of the lattice ethanol molecules (Scheme 2). The second step in the TGA plots is an extremely sharp *exo*thermic effect at 177 and 196 °C, and is seen as an abrupt weight deviation due to the so-called "jet" effect, which is explained by a drastic energy release upon heating (Fig. 4). This step in the TGA plot of **2** is a result of the release of nitrogen gas by losing all the azides as well as the decomposition of the ligands **L** followed by the full reduction of

cobalt(III) with the formation of elemental cobalt as a final residue (Scheme 2). Elemental cobalt exists in either hexagonal or cubic phase. According to the X-ray powder diffraction pattern (Fig. 5), the obtained elemental cobalt sample exhibits a mixture of both phases.

The same decomposition step in the TGA plot of **1** is also a result of the release of nitrogen gas by, however, losing one azide followed by the partial reduction of cobalt(III) only up to cobalt(II) (Scheme 2). The last thermal decomposition step of **1** is attributed to the *exo*thermic decomposition of the ligands **L** and remaining azide at about 215 °C with the formation, as evidenced from X-ray powder diffraction analysis (Fig. 5), of a mixture of $CoCl_2$ and Co_2N as a final residue (Scheme 2). Thus, the presence of the chloride anion in the structure of **1** plays a pivotal role both in the thermal decomposition pathway as well as in the lowering of the energy release.

In order to provide additional knowledge on the newly synthetized cobalt complexes, we have performed the preliminary theoretical studies predominantly at the DFT/BLYP-D3/TZP level of theory as implemented in the Amsterdam Density Functional (ADF) package [30,31]. Since both structures contain weakly bonded moieties, we have decided to apply the BLYP-D3 functional, which appeared to provide a reasonable description of non-covalent interactions [32–34].

As far as octahedral cobalt(III) complexes are concerned, we have found, in line with the experimental outcomes, that the singlet (S = 0) diamagnetic species is of the lowest energy in comparison with the corresponding open shell conformations (S = 1 and 2) (Fig. 6). The open shell species with the triplet (S = 1) and quintet (S = 2) multiplicities are significantly less stable (Fig. 6). The same trend is valid when considering the hybrid B3LYP functional, namely the closed shell $[CoL_2(N_3)_2]^+$ is more stable than the corresponding open shell isomers by about 15 kcal/mol. Such relation can originate from the shortest, and hence the strongest, Co–N distances noted for the diamagnetic cobalt(III) isomer (Fig. 6). Considering the neutral cobalt(II) complex $[CoL_2(N_3)_2]$ we have found that the doublet (S = 1/2) state is the most stable. The unpaired electron of $[CoL_2(N_3)_2]$ was found to be located predominantly at cobalt as suggested by the calculated spin density contour (Fig. 7). Our calculations suggest that the oxidation reaction occurs at the cobalt center Co(II) → Co(III) and could proceed from the neutral octahedral $[CoL_2(N_3)_2]$ complex to the corresponding cationic $[CoL_2(N_3)_2]^+$ species. The ionization potential (I_p) of $[CoL_2(N_3)_2]$, approximated by

the Koopmans theorem ($I_p = -E_{SOMO}$), is quite low (3.25 eV), suggesting that the oxidation process $[CoL_2(N_3)_2] \rightarrow [CoL_2(N_3)_2]^+$ is facile.

In order to shed some light on the stability of **1** we have performed the charge and energy decomposition study by means of the ETS-NOCV method [35–37]. We have chosen the cluster models of **1** (Fig. 8 and 9, top row). It was found that the bonding within the ion pair of $[CoL_2(N_3)_2]^+$ and N_3^-, which is, as expected, electrostatically dominated, is characterized by a very low interaction energy (ΔE_{int} = –80.36 kcal/mol) (Fig. 8, left panel). It appeared to be far stronger in comparison with the weak noncovalent interaction formed by ethanol (ΔE_{int} = –5.02 kcal/mol) (Fig. 8, right panel), and weaker with respect to dative bonding of **L** (ΔE_{int} = –94.00 kcal/mol) (Fig. 9, left panel). It should be noted that these relations correlate qualitatively well with the experimental thermal decomposition sequence (Scheme 2), namely ethanol, which is weakly bonded through dispersion forces, is detached at first stage followed by nitrogen release, originating likely from the non-bonded N_3^-, and decomposition of **L**. According to the TGA experimental data some of the N_3^- ligands in **1** survived after the second decomposition step what could be attributed to the strongest N_3^- bonding with the cobalt(III) ion (ΔE_{int} = –123.86 kcal/mol) (Fig. 8, right panel), as it was evidenced from the ETS-NOCV calculations. Dispersion stabilization (ΔE_{disp}) was found to be dominant in the case of the weakest interaction between ethanol and $[CoL_2(N_3)_2]^+$, whereas the electrostatic contribution (ΔE_{elstat}) is prevalent over the charge transfer term (ΔE_{orb}) for the N_3^- and **L** bonds (Fig. 8 and 9). Considering changes in the electron density, one can state that both N_3^- and **L** in $[CoL_2(N_3)_2]^+$ form typical dative bonds, where donation (N → Co) and back-donation (Co → π*) are noted from the contours of $\Delta\rho_{orb}$ (Fig. 9, bottom row), whereas the CH → π* charge transfer is seen upon interaction of ethanol with $[CoL_2(N_3)_2]^+$ (Fig. 8). Finally, the internal polarizations occur due to the ionic interaction of N_3^- and $[CoL_2(N_3)_2]^+$ (Fig. 8).

3. Experimental

3.1. Physical measurements

^{1}H NMR spectra in DMSO-d_6 were obtained on a Bruker Avance 300 MHz spectrometer at 25 °C and were recorded at 299.948 MHz. Chemical shifts are reported with reference to $SiMe_4$. Thermogravimetric

analyses (TG) were performed by a SDT 2960 Simultaneous DTA-TGA instrument from room temperature to 400 °C with a 10 °C min^{-1} heating rate. Differential scanning calorimetry (DSC) measurements were carried out using a Mettler Toledo DSC 820 instrument from room temperature to 500 °C with a 10 °C min^{-1} heating rate. An aluminium crucible was loaded with 15 mg of a crystalline sample. Elemental analyses were performed on a Thermoquest Flash EA 1112 Analyzer from CE Instruments.

*3.2. Synthesis of **1** and **2***

A solution of **L** (0.10 mmol, 23.2 mg or 0.20 mmol, 46.4 mg) in EtOH (5 mL) was added dropwise under vigorous stirring to a mixture of $CoCl_2 \cdot 6H_2O$ (0.10 mmol, 23.8 mg) and NaN_3 (0.20 mmol, 13.0 mg) in a mixture of EtOH (5 mL) and CH_3CN (10 mL). The mixture was stirred under reflux for 15 min and filtered. Crystals suitable for single crystal X-ray analysis were obtained on standing with slow evaporation of the solvent.

1. Dark red plate-like crystals. Yield: 28.4 mg (82%). ^{1}H NMR, δ: 1.08 (t, $^3J_{H,H}$ = 7.0 Hz, 3H, CH_3, EtOH), 3.39 (q, $^3J_{H,H}$ = 7.0 Hz, 2H, CH_2, EtOH), 7.37–7.62 (m, 12H, L), 7.98 (t, $^3J_{H,H}$ = 7.7 Hz, 2H, L), 8.28–8.44 (m, 4H, L), 8.68–8.82 (m, 6H, L) ppm. *Anal*. Calc. for $C_{34}H_{30}Cl_{0.451}CoN_{11.647}O$ (692.67): C 58.96, H 4.37, N 23.55. Found: C 59.18, H 4.52, N 23.73%.

2. Dark red block-like crystals. Yield: 37.7 mg (87%). ^{1}H NMR, δ: 1.10 (t, $^3J_{H,H}$ = 7.0 Hz, 7.5H, CH_3, EtOH), 3.41 (q, $^3J_{H,H}$ = 7.0 Hz, 5H, CH_2, EtOH), 7.39–7.65 (m, 12H, L), 8.01 (t, $^3J_{H,H}$ = 7.7 Hz, 2H, L), 8.29–8.42 (m, 4H, L), 8.70–8.84 (m, 6H, L) ppm. *Anal*. Calc. for $C_{37}H_{39}CoN_{13}O_{2.5}$ (764.74): C 58.11, H 5.14, N 23.81. Found: C 58.23, H 5.21, N 23.69%.

3.3. X-Ray powder diffraction

X-Ray powder diffraction was carried out using a Mar345 image plate detector using Mo-Kα radiation (Xenocs Fox3D mirror).

3.4. Single-crystal X-ray diffraction

The X-ray data for **1** and **2** were collected at 150(2) and 200(2) K, respectively, on a Mar345 image plate detector using Mo-Kα radiation (Xenocs Fox3D mirror). The data were integrated with the CrysAlis(Pro) software [38]. The implemented empirical absorption correction was applied. The structures of **1** and **2** were solved by SHELXS97 [39] and refined by full-matrix least squares on $|F^2|$, using SHELXL2014/7 [40]. Non-hydrogen atoms were anisotropically refined and the hydrogen atoms were placed on calculated positions in riding mode with temperature factors fixed at 1.2 times U_{eq} of the parent atoms. Crystals of **2** diffracted poorly and a data cut-off of 1.1 Å had to be imposed during integration. Further, the crystals of **2** were also found to be twinned around the reciprocal *c* axis and the TWINROTMAT procedure in PLATON [41] was used to deconvolute the two twin domains (refined twin fraction about 17%). Additionally, **2** contains two cavities of 194 Å^3 with non-discrete solvent molecules, these cavities were treated with PLATON-SQUEEZE [41] to account for the 69 electrons found in both voids. Figures were generated using the program Mercury [42].

Crystal data for 1. $C_{32}H_{24}CoN_{10}$, C_2H_6O, 0.549N_3, 0.451Cl; M_r = 692.61 g mol^{-1}, triclinic, space group *P*–1, a = 10.6062(9), b = 10.6514(10), c = 14.6168(10) Å, α = 83.913(7), β = 75.124(7), γ = 88.948(7)°, V = 1586.9(2) Å^3, Z = 2, ρ = 1.450 g cm^{-3}, μ(Mo-Kα) = 0.628 mm^{-1}, reflections: 15970 collected, 5693 unique, R_{int} = 0.055, R_1(all) = 0.0782, wR_2(all) = 0.1500.

Crystal data for 2. $C_{32}H_{24}CoN_{10}$, N_3; M_r = 649.57 g mol^{-1}, triclinic, space group *P*–1, a = 8.423(2), b = 12.481(3), c = 31.83(1) Å, α = 83.39(2), β = 82.84(2), γ = 74.64(2)°, V = 3189.7(15) Å^3, Z = 4, ρ = 1.353 g cm^{-3}, μ(Mo-Kα) = 0.583 mm^{-1}, reflections: 4752 collected, 4752 unique, R_{int} = 0.000, R_1(all) = 0.2724, wR_2(all) = 0.3712.

CCDC 1482306 (**1**) and 1482307 (**2**) contain the supplementary crystallographic data. These data can be obtained free of charge via http://www.ccdc.cam.ac.uk/conts/retrieving.html, or from the Cambridge Crystallographic Data Centre, 12 Union Road, Cambridge CB2 1EZ, UK; fax: (+44) 1223-336-033; or e-mail: deposit@ccdc.cam.ac.uk.

3.4. DFT calculations

We have performed the DFT calculations based on the BLYP-D3/TZP as implemented in the ADF package [30,31]. In addition the dispersion corrected (D3) B3LYP functional was applied to check the sensitivity of our results.

3.5. ETS-NOCV bonding analysis

Natural Orbitals for Chemical Valence (NOCV) are eigenvectors that diagonalize deformation density matrix [35–37]. It was shown that the natural orbitals for chemical valence pairs (ψ_{-k},ψ_k) decompose the differential density $\Delta\rho$ into NOCV-contributions ($\Delta\rho_k$):

$$\Delta\rho(r) = \sum_{k=1}^{M/2} v_k[-\psi_{-k}^2(r) + \psi_k^2(r)] = \sum_{k=1}^{M/2} \Delta\rho_k(r),$$

where v_k and M stand for the NOCV eigenvalues and the number of basis functions, respectively. Visual inspection of deformation density plots ($\Delta\rho_k$) helps to attribute symmetry and direction of the charge flow. In addition, these pictures are enriched by providing the energetic estimations, $\Delta E_{orb}(k)$, for each $\Delta\rho_k$ within ETS-NOCV scheme [35–37]. The exact formula, which links the ETS and NOCV methods, will be given in the next paragraph, after we briefly present the basic concept of ETS scheme. In this method the total bonding energy ΔE_{int} between interacting fragments, exhibiting geometry as in the combined complex, is divided into the three components: $\Delta E_{\text{int}} = \Delta E_{\text{elstat}} + \Delta E_{\text{Pauli}} + \Delta E_{\text{orb}}$. The first term, ΔE_{elstat}, corresponds to the classical electrostatic interaction between the promoted fragments as they are brought to their positions in the final complex. The second term, ΔE_{Pauli}, accounts for the repulsive Pauli interaction between occupied orbitals on the two fragments in the combined molecule. Finally, the last stabilizing term, ΔE_{orb}, represents interactions between the occupied molecular orbitals of one fragment with the unoccupied molecular orbitals of the other fragment as well as mixing of occupied and virtual orbitals within the same fragment (inner-fragment polarization). The orbital interaction contribution may be further linked to the electronic bonding effect coming from the formation of a chemical bond. In the combined ETS-NOCV scheme [35–37] the orbital interaction term, ΔE_{orb}, is expressed in terms of NOCV's eigenvalues (v_k) as:

$$\Delta E_{orb} = \sum_{k} \Delta E_{orb}(k) = \sum_{k=1}^{M/2} v_k [-F^{TS}_{-k,-k} + F^{TS}_{k,k}],$$

where $F^{TS}_{k,k}$ are diagonal Kohn-Sham matrix elements defined over NOCV with respect to the transition state (TS) density at the midpoint between density of the molecule and the sum of fragment densities. The above components $\Delta E_{\mathrm{orb}}(k)$ provide the energetic estimation of $\Delta\rho_k$ that may be related to the importance of a particular electron flow channel for the bonding between the considered molecular fragments. ETS-NOCV analysis was done based on the Amsterdam Density Functional (ADF) package [30,31] in which this scheme was implemented.

4. Conclusions

In summary, we have synthesised two mononuclear heteroleptic cobalt(III) complexes, $[CoL_2(N_3)_2](N_3)_{0.55}Cl_{0.45}\cdot EtOH$ (**1**) and $[CoL_2(N_3)_2]N_3\cdot 2.5EtOH$ (**2**), with 5-phenyl-2,2'-bipyridine (**L**) and N_3^-, reacting one or two equivalents of **L**, respectively, with a mixture of one equivalent of $CoCl_2$ and two equivalents of NaN_3. According to X-ray diffraction analysis, both structures reveal that the cobalt(III) atom is linked to two **L** and two N_3^- anions and are additionally stabilized by weak intermolecular interactions. ^{1}H NMR spectroscopy and DFT calculations have confirmed the diamagnetic nature of both **1** and **2**.

The molecules of **1** and **2** are stable up to 63 and 84°C and decompose in three and two clearly defined steps, respectively. Both decomposition pathways start with the *endo*thermic release of EtOH molecules, while the second step corresponds to an abrupt weight loss at 177 (**1**) and 196 °C (**2**), due to the so-called "jet" effect. The final residue after thermal decomposition of **2** corresponds to a mixture of hexagonal and cubic phases of elemental cobalt, while the formation of a mixture of $CoCl_2$ and Co_2N, as a final residue, was found upon thermal decomposition of **1**. The charge and energy decomposition ETS-NOCV-based results allowed to rationalize the decomposition pathways. Both compounds are potential materials for the release of thermal energy and in-depth studies of their controlled detonation properties are anticipated.

Acknowledgements

We thank WBI (Belgium) for post-doctoral positions allocated to D. A. Safin. We also acknowledge Fonds National de la Recherche Scientifique (FNRS, Belgium) for financial support. DFT calculations were performed using the PL-Grid Infrastructure and resources provided by the ACC Cyfronet AGH (Cracow, Poland).

References

[1] E.A. Betterton, Crit. Rev. Environ. Sci. Technol. 33 (2003) 423.

[2] D.R. Lide, Handbook of Chemistry and Physics, 87th ed., CRC Press, Boca Raton, FL (1998) pp. 4–55.

[3] P. Patnaik, Handbook of Inorganic Chemicals, The McGraw-Hill Companies Inc., USA (2003) pp. 460–461.

[4] L.-Y. Wang, B. Zhao, C.-X. Zhang, D.-Z. Liao, Z.-H. Jiang, S.-P. Yan, Inorg. Chem. 42 (2003) 5804.

[5] X.-Y. Wang, L. Wang, Z.-M. Wang, S. Gao, J. Am. Chem. Soc. 128 (2006) 674.

[6] X.-T. Wang, Z.-M. Wang, S. Gao, Inorg. Chem. 46 (2007) 10452.

[7] G.H. Palenik, Acta Crystallogr. 17 (1964) 360.

[8] C.E. Housecroft, E.C. Constable, Chem. Soc. Rev. 44 (2015) 8386.

[9] D.A. Safin, J. Frost, M. Murugesu, Dalton Trans. 44 (2015) 20287.

[10] F.H. Case, E. Koft, J. Am. Chem. Soc. 81 (1959) 905.

[11] E.I. Lerner, S.J. Lippard, Inorg. Chem. 16 (1977) 1537.

[12] A.M. Garcia, D.M. Bassani, J.-M. Lehn, G. Baum, D. Fenske, Chem. Eur. J. 5 (1999) 1234.

[13] D.A. Safin, Y. Xu, I. Korobkov, D.L. Bryce, M. Murugesu, CrystEngComm 15 (2013) 10419.

[14] D.A. Safin, N.A. Tumanov, A.A. Leitch, J.L. Brusso, Y. Filinchuk, M. Murugesu, CrystEngComm 17 (2015) 2190.

[15] D.A. Safin, K.M.N. Burgess, I. Korobkov, D.L. Bryce, M. Murugesu, CrystEngComm 14 (2014) 3466.

[16] D.A. Safin, R.J. Holmberg, K.M.N. Burgess, K. Robeyns, D.L. Bryce, M. Murugesu, Eur. J. Inorg. Chem. (2015) 441.

[17] D.A. Safin, A. Pialat, I. Korobkov, M. Murugesu, Chem. Eur. J. 21 (2015) 6144.

[18] D.A. Safin, A. Pialat, A.A. Leitch, N.A. Tumanov, I. Korobkov, Y. Filinchuk, J.L. Brusso, M. Murugesu, Chem Commun. 51 (2015) 9547.

[19] D.A. Safin, P.M.J. Szell, A. Keller, I. Korobkov, D.L. Bryce, M. Murugesu, New J. Chem. 39 (2015) 7147.

[20] V.N. Kozhevnikov, D.N. Kozhevnikov, O.V. Shabunina, V.L. Rusinov, O.N. Chupakhin, Tetrahedron Lett. 46 (2005) 1791.

[21] D.N. Kozhevnikov, O.V. Shabunina, D.S. Kopchuk, P.A. Slepukhin, V.N. Kozhevnikov, Tetrahedron Lett. 47 (2006) 7025.

[22] D.A. Safin, M.P. Mitoraj, K. Robeyns, Y. Filinchuk, C.M.L. Vande Velde, Dalton Trans. 44 (2015) 16824.

[23] D.A. Safin, C.M.L. Vande Velde, M.G. Babashkina, K. Robeyns, Y. Filinchuk, New J. Chem. 40 (2016) 6156.

[24] D.A. Safin, K. Robeyns, M.G. Babashkina, C.M.L. Vande Velde, Y. Filinchuk, Cryst. Growth Des. 16 (2016) 3763.

[25] J. Bjerrum, J.P. McReynolds, Inorg. Synth. 2 (1946) 216.

[26] M. Calligaris, Coord. Chem. Rev. 248 (2004) 351.

[27] J.A. Davies, The Coordination Chemistry of Sulfoxides with Transition Metals. In *Advances in Inorganic Chemistry and Radiochemistry*. Eds. H.J. Emeléus, A.G. Sharpe. Academic Press: New York, 24 (1981) 115–187.

[28] F.H. Allen, Acta Crystallogr. B58 (2002) 380.

[29] CSD version 5.37 (November 2015 + 3 updates).

[30] G. te Velde, F.M. Bickelhaupt, E.J. Baerends, C. Fonseca Guerra, S.J.A. van Gisbergen, J.G. Snijders, T. Ziegler, J. Comput. Chem. 22 (2001) 931 and references therein.

[31] E.J. Baerends, J. Autschbach, D. Bashford, A. Bérces, F.M. Bickelhaupt, C. Bo, P.M. Boerrigter, L. Cavallo, D.P. Chong, L. Deng, R.M. Dickson, D.E. Ellis, M. van Faassen, L. Fan, T.H. Fischer, C. Fonseca Guerra, A. Ghysels, A. Giammona, S.J.A. van Gisbergen, A.W. Götz, J.A. Groeneveld, O.V. Gritsenko, M. Grüning, F.E. Harris, P. van den Hoek, C.R. Jacob, H. Jacobsen, L. Jensen, G. van Kessel, F. Kootstra, M.V. Krykunov, E. van Lenthe, D.A. McCormack, A. Michalak, M. Mitoraj, J. Neugebauer, V.P. Nicu, L. Noodleman, V.P. Osinga, S. Patchkovskii, P.H.T. Philipsen, D. Post, C.C. Pye, W. Ravenek, J.I. Rodríguez, P. Ros, P.R.T. Schipper, G. Schreckenbach, M. Seth, J.G. Snijders, M. Solà, M. Swart, D. Swerhone, G. te Velde, P. Vernooijs, L. Versluis, L. Visscher, O. Visser, F.

Wang, T.A. Wesolowski, E.M. van Wezenbeek, G. Wiesenekker, S.K. Wolff, T.K. Woo, A.L. Yakovlev, T. Ziegler, ADF2012.01, Theoretical Chemistry, Vrije Universiteit, Amsterdam.

[32] T. van der Wijst, C. Fonseca Guerra, M. Swart, F.M. Bickelhaupt, B. Lippert, Angew. Chem. Int. Ed. 48 (2009) 3285.

[33] C. Fonseca Guerra, T. van der Wijst, J. Poater, M. Swart, F.M. Bickelhaupt, Theor. Chem. Acc. 125 (2010) 245.

[34] W. Gao, H. Feng, X. Xuan, L. Chen, J. Mol. Model. 18 (2012) 4577.

[35] M. Mitoraj, A. Michalak, J. Mol. Model. 13 (2007) 347.

[36] A. Michalak, M. Mitoraj, T. Ziegler, J. Phys. Chem. A 112 (2008) 1933.

[37] M. Mitoraj, A. Michalak, T. Ziegler, J. Chem. Theory Comput. 5 (2009) 962.

[38] Rigaku Oxford Diffraction, CrysAlis(Pro) Software system, version 1.171.37.31, Rigaku Corporation, Oxford, UK (2014).

[39] G.M. Sheldrick, Acta Crystallogr. A64 (2008) 112.

[40] G.M. Sheldrick, SHELXL2014/7, University of Göttingen, Germany (2014).

[41] A.L. Spek, Acta Crystallogr. D65 (2009) 148.

[42] I.J. Bruno, J.C. Cole, P.R. Edgington, M. Kessler, C.F. Macrae, P. McCabe, J. Pearson, R. Taylor, Acta Crystallogr. B58 (2002) 389.

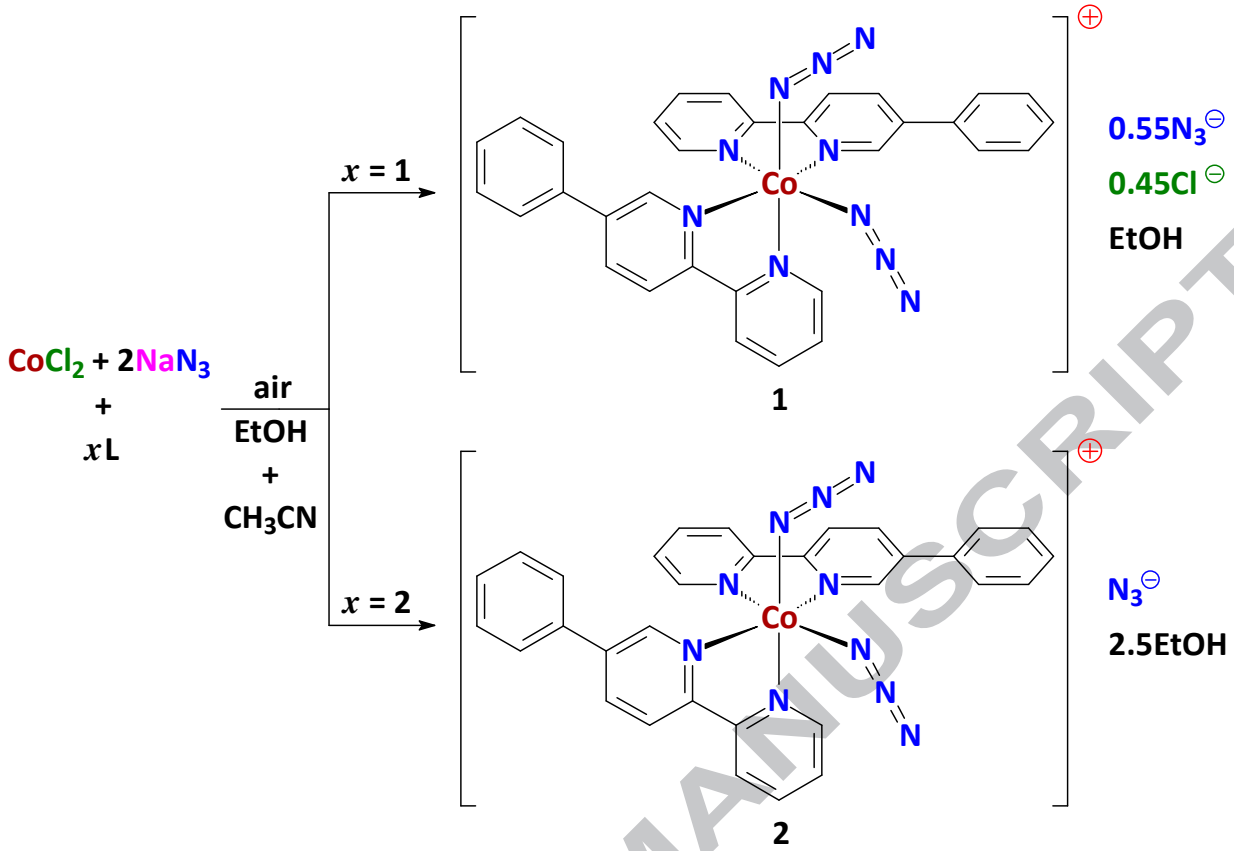

Scheme 1. Synthesis of **1** and **2**.

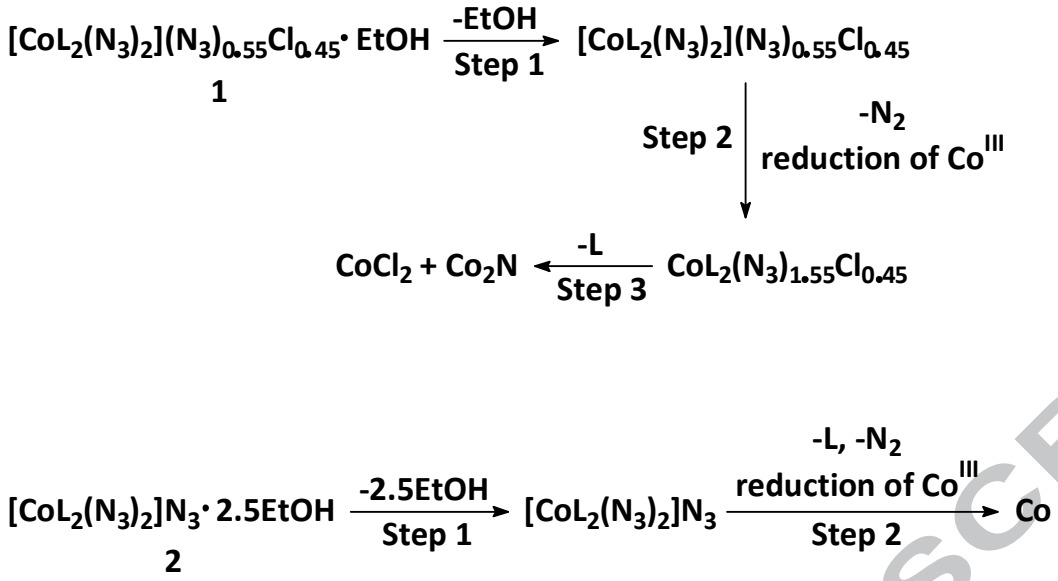

Scheme 2. Thermal decomposition pathways of **1** and **2**.

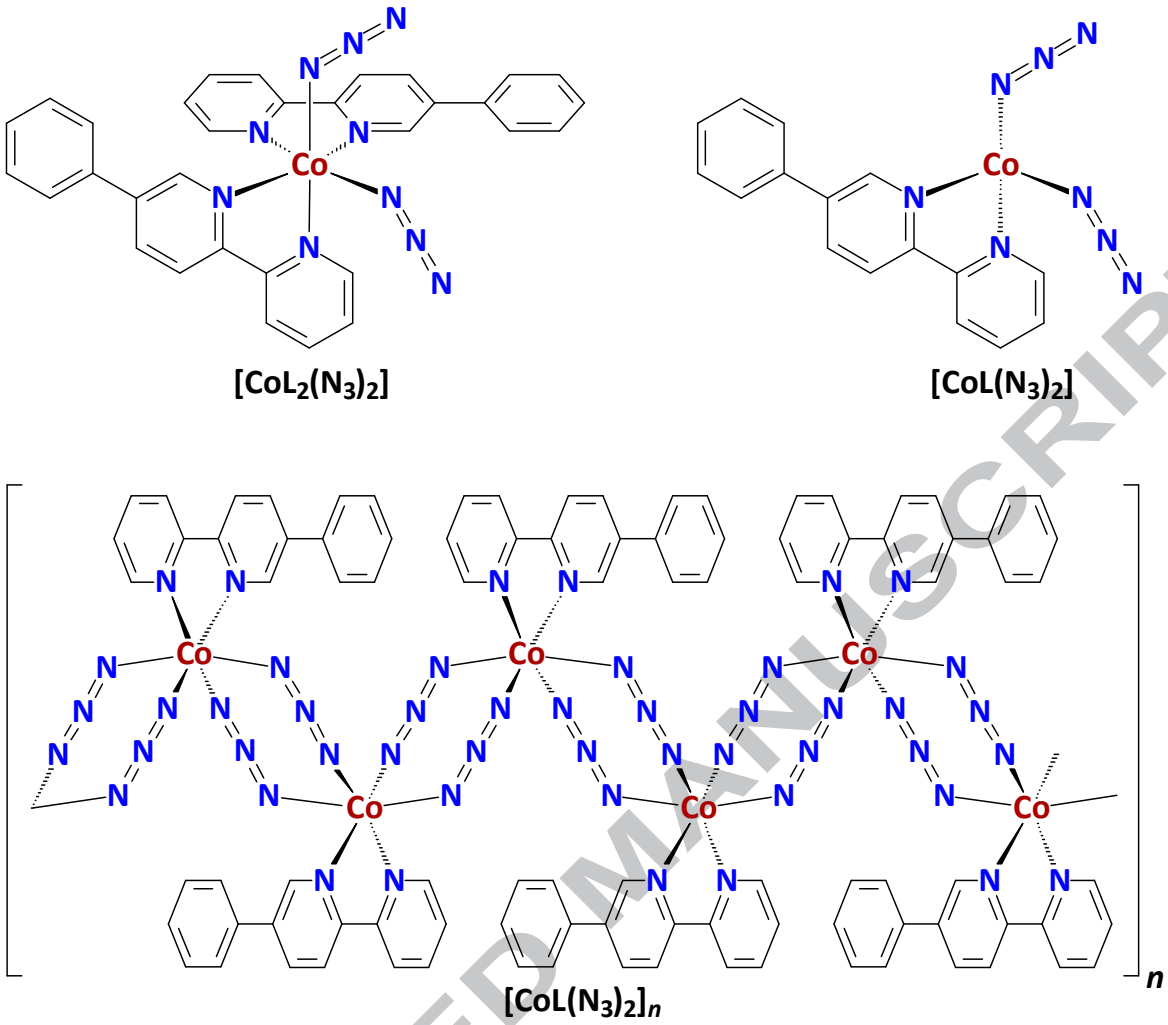

Chart 1.

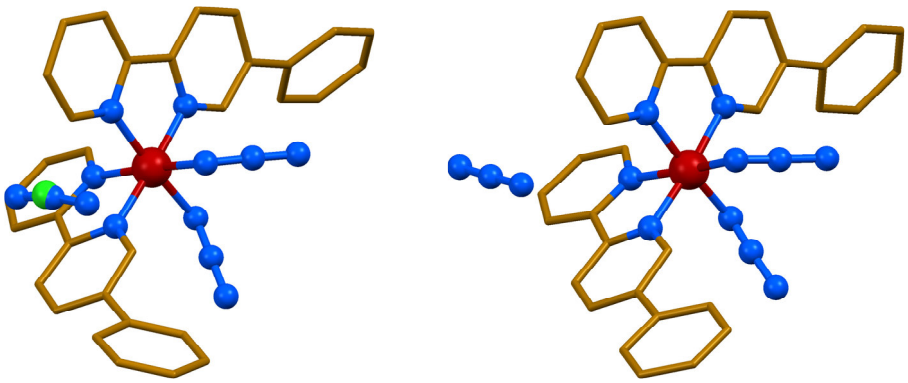

Fig. 1. Ball and stick molecular structures of **1** (left) and **2-I** (right). Hydrogen atoms, and the ethanol molecule in **1**, were omitted for clarity. Colour code: C = gold, N = blue, Cl = green, Co = dark red.

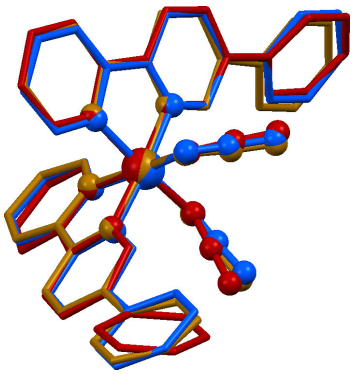

Fig. 2. Ball and stick molecule overlay of the $[CoL_2(N_3)_2]^+$·cations extracted from the structures of **1** (dark red), **2-I** (blue) and **2-II** (gold). Hydrogen atoms were omitted for clarity.

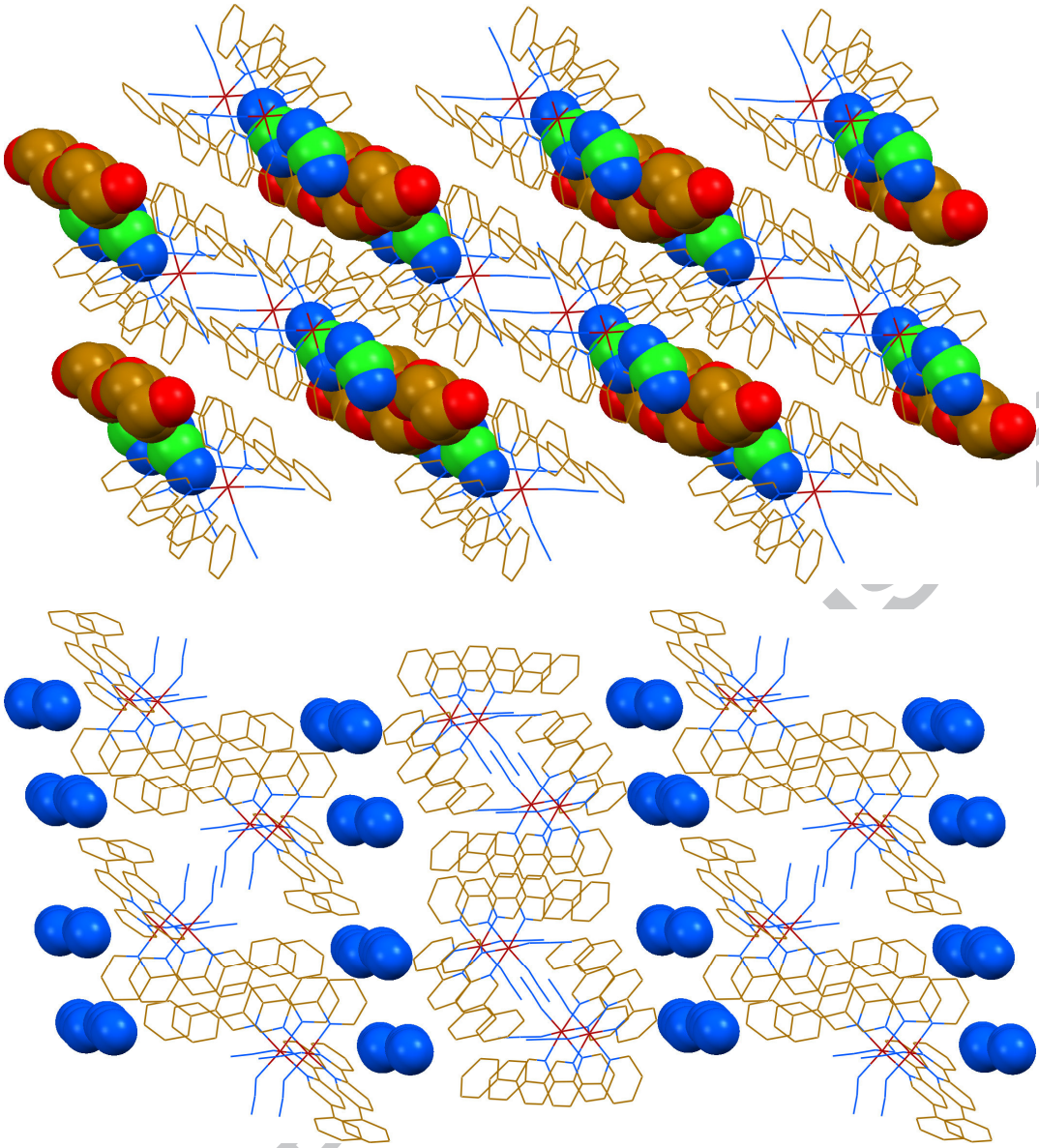

Fig. 3. Wireframe and spacefill crystal packing of **1** (top) and **2** (bottom) along the *b* and *a* axis, respectively. Ethanol molecules in **1** are shown disordered over two positions. Hydrogen atoms were omitted for clarity. Colour code: C = gold, N = blue, Cl = green, Co = dark red.

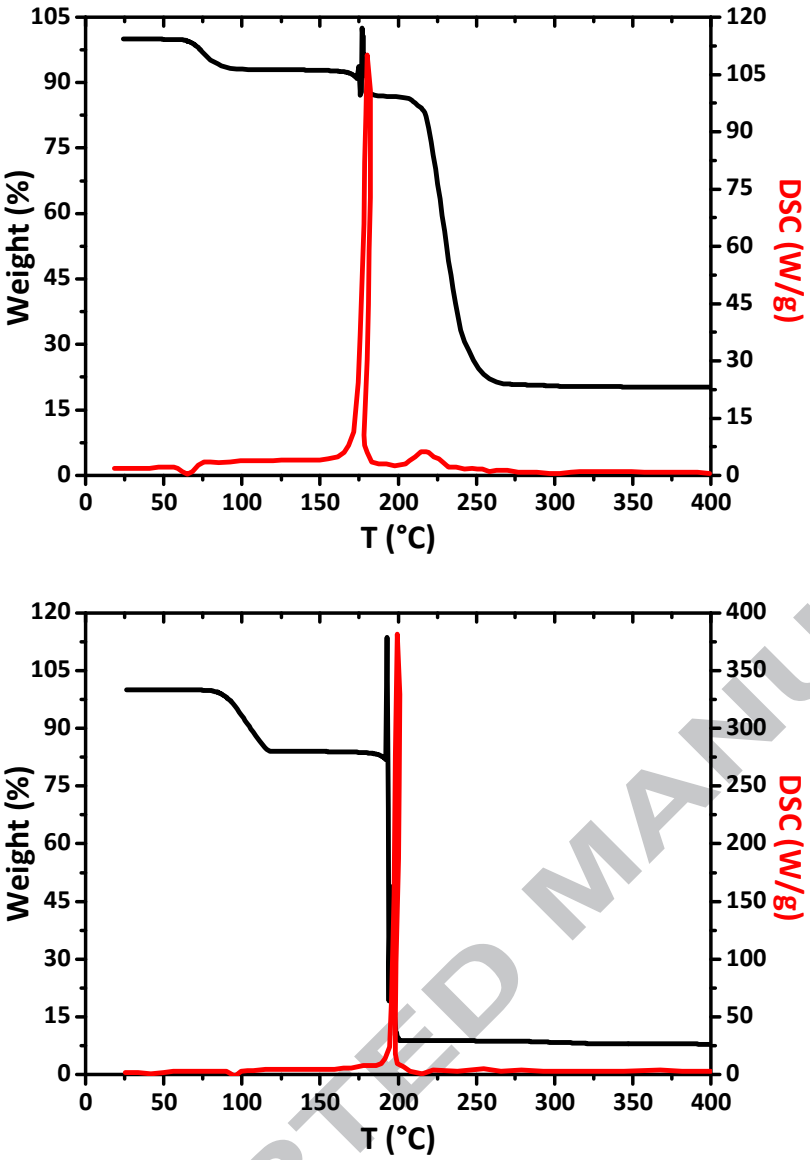

Fig. 4. TG (black) and DSC (red) analyses for **1** (top) and **2** (bottom).

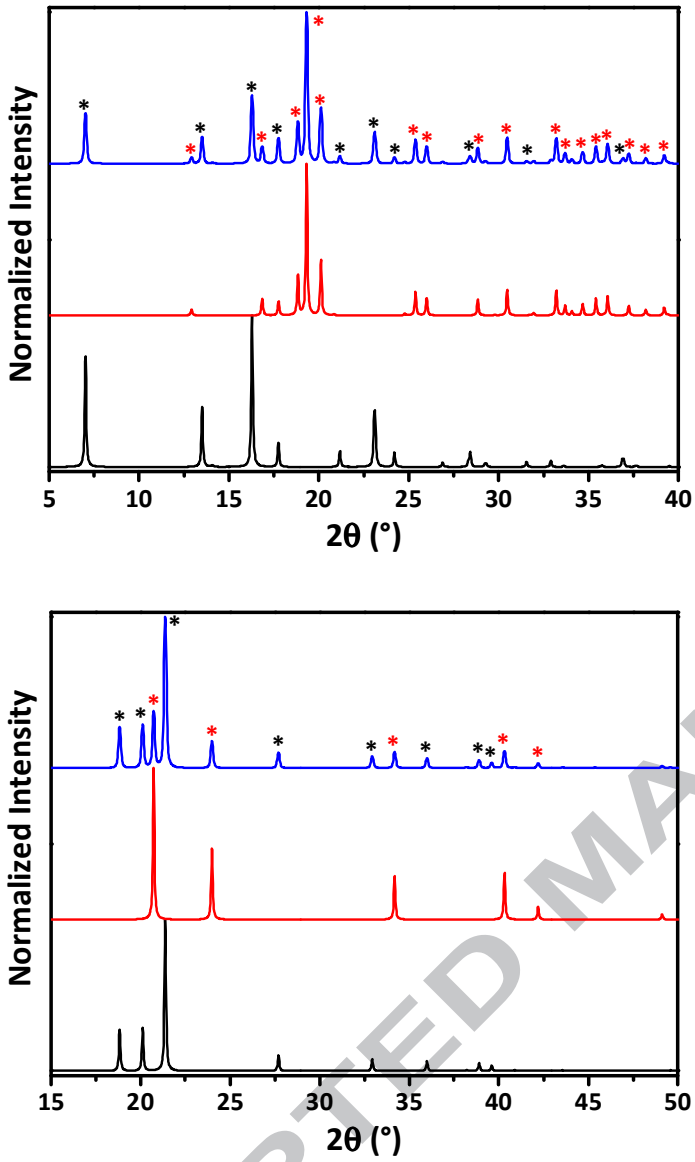

Fig. 5. Experimental (blue) X-ray powder diffraction patterns of final residues obtained after TG analyses of **1** (top) and **2** (bottom). Calculated for $CoCl_2$ (black) and Co_2N (red) X-ray powder diffraction patterns (top). Calculated for hexagonal (black) and cubic (red) X-ray powder diffraction patterns of elemental cobalt (bottom).

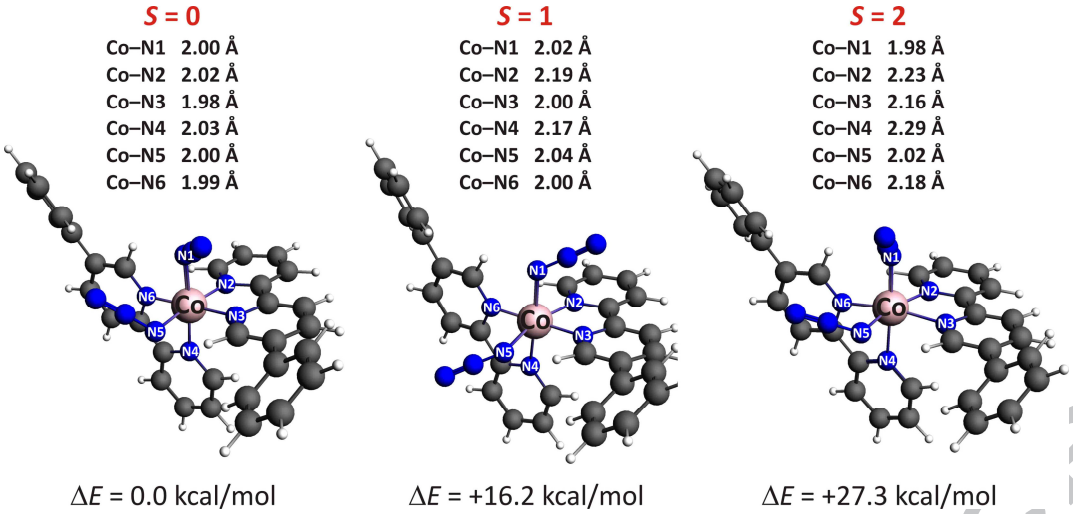

Fig. 6. The lowest energy conformations of the cobalt(III) complexes $[CoL_2(N_3)_2]^+$, characterized by various spin states based on the ADF/BLYP-D3/TZP calculations.

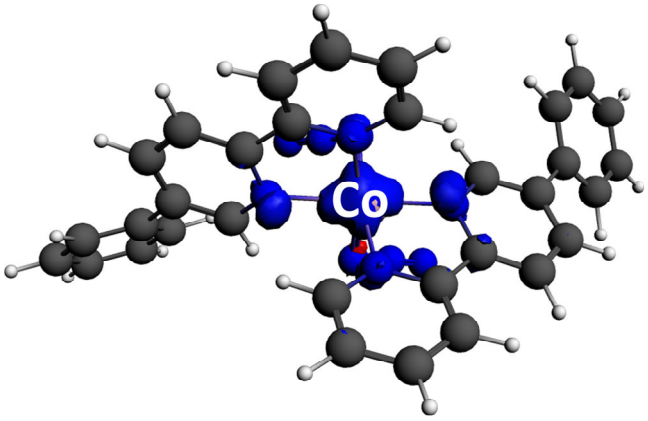

Fig. 7. Calculated spin density of the neutral $[CoL_2(N_3)_2]$ molecule based on the ADF/BLYP-D3/TZP calculations.

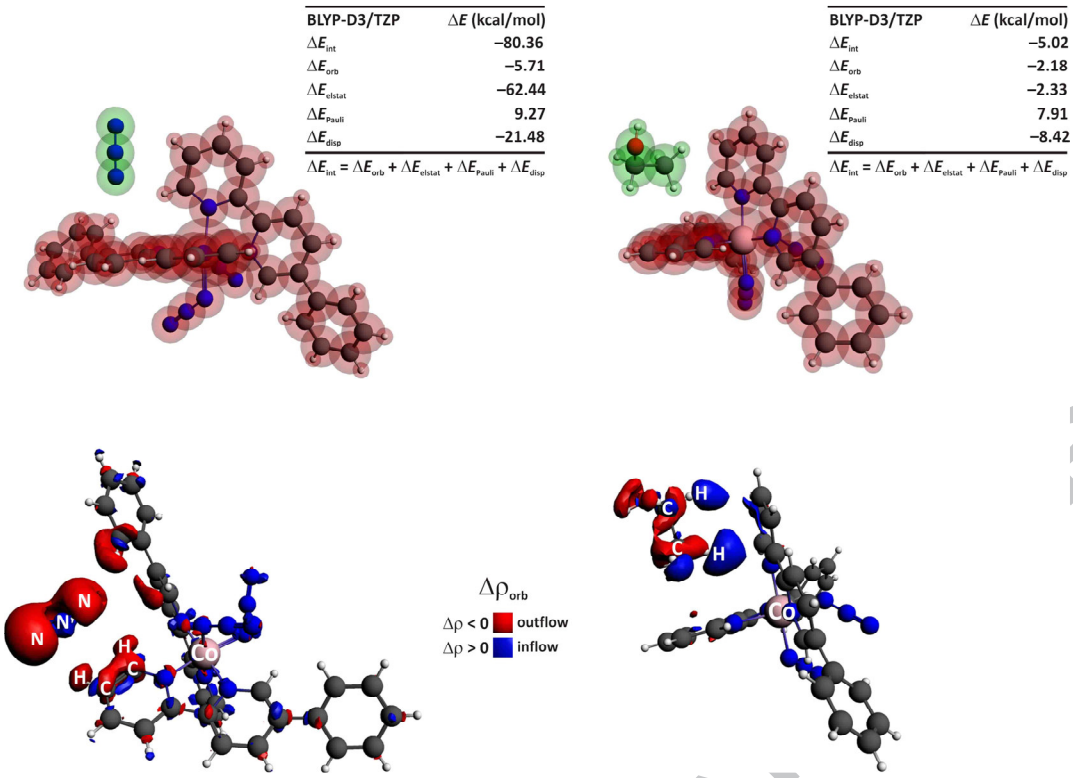

Fig. 8. ETS-NOCV energy decomposition results (top row) and the overall deformation density $\Delta\rho_{orb}$ (bottom rom), describing interaction between $[CoL_2(N_3)_2]^+$ and N_3^- (left), and $[CoL_2(N_3)_2]^+$ and ethanol (right).

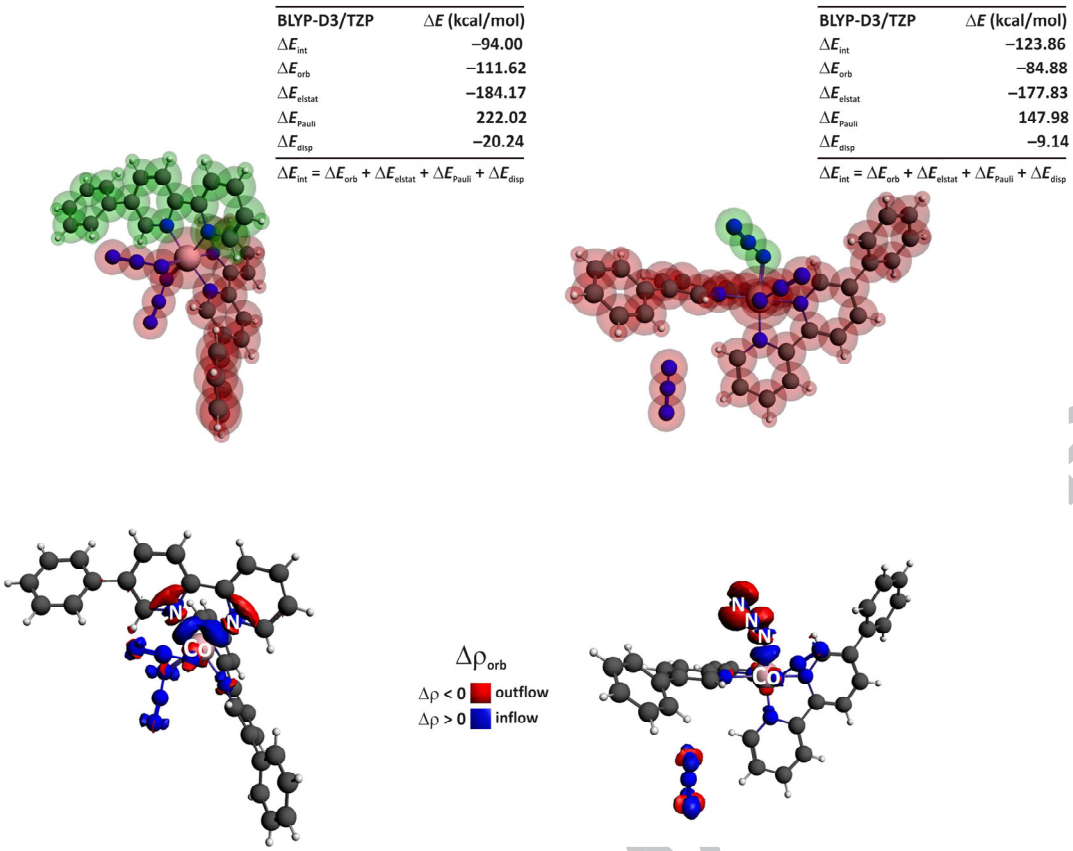

Fig. 9. ETS-NOCV energy decomposition results (top row) and the overall deformation density $\Delta\rho_{orb}$ (bottom rom), describing interaction between $[CoL(N_3)_2]^+$ and **L** (left), and $[CoL_2(N_3)]^{2+}$ and axial N_3^- (right).

Table 1

Selected bond lengths (Å) and angles (°) for $[CoL_2(N_3)_2]^+$ in the structures of **1**, **2-I** and **2-II**.

	1	**2-I**	**2-II**
Bond lengths			
Co–N(Py)	1.930(3), 1.943(3)	1.94(2), 1.96(2)	1.95(2)
Co–N($Py_{terminal}$)	1.951(3), 1.953(3)	1.96(2), 1.98(3)	1.94(2), 1.97(2)
Co–N_3	1.934(3), 1.936(3)	1.89(3), 2.04(3)	1.91(3), 1.98(3)
Bond angles			
N(Py)–Co–N(Py_{endo})	82.85(14), 82.86(13)	82.0(10), 82.4(9)	81.9(8), 83.1(9)
N(Py)–Co–N(Py_{exo})	91.48(13), 94.78(13), 95.90(13), 177.32(13)	89.9(10), 93.6(10), 96.5(10), 175.7(9)	88.9(10), 94.1(10), 94.2(9), 175.3(9)
N(Py)–Co–N_3	87.74(13), 89.33(13), 89.48(14), 90.44(13), 91.71(14), 91.92(13), 174.43(14), 174.78(14)	80.8(11), 87.5(11), 90.3(11), 90.6(11), 91.8(11), 92.1(10), 167.5(11), 173.7(11)	85.9(11), 87.4(10), 89.6(10), 91.4(9), 92.3(10), 92.8(11), 170.7(11), 172.1(10)
N_3–Co–N_3	91.95(13)	102.6(12)	98.7(12)
Dihedral angles			
Py···$Py_{terminal}$	5.65(18), 7.33(18)	2.2(14), 6.7(14)	3.7(12), 6.5(13)
Py···Ph	38.55(19), 44.22(19)	11.4(11), 30.3(11)	21.7(11), 32.5(11)
$Py_{terminal}$···Ph	43.55(19), 45.7(2)	9.6(13), 30.7(13)	18.6(11), 34.1(12)

Table 2

Hydrogen bond and weak interaction lengths (Å) and angles (°) for **1** and **2**.

	D–H···A	*d*(D–H)	*d*(H···A)	*d*(D···A)	∠(DHA)
1[a]	O(53)–H(53)···N(73)$^{\#1}$	0.84	2.28	3.036(19)	149
	C(3)–H(3)···N(71)$^{\#1}$	0.95	2.53	3.274(12)	135
	C(4)–H(4)···Cl(61)$^{\#1}$	0.95	2.67	3.395(8)	134
	C(6)–H(6)···N(43)$^{\#2}$	0.95	2.45	3.213(6)	138
	C(23)–H(23)···Cl(61)$^{\#3}$	0.95	2.77	3.418(8)	126
	C(23)–H(23)···N(73)$^{\#3}$	0.95	2.43	3.179(17)	136
	C(26)–H(26)···N(71)$^{\#4}$	0.95	2.33	3.261(12)	166
	C(33)–H(33)···Cl(61)$^{\#4}$	0.95	2.71	3.575(7)	151
	C(33)–H(33)···N(71)$^{\#4}$	0.95	2.55	3.494(11)	172
	C(35)–H(35)···N(71)$^{\#1}$	0.95	2.59	3.215(13)	123
	C(38)–H(38)···N(73)$^{\#5}$	0.95	2.36	3.29(2)	168
2[b]	C(13)–H(13)···N(46)$^{\#1}$	0.95	2.41	3.30(4)	156
	C(15)–H(15)···N(43)$^{\#2}$	0.95	2.56	3.39(3)	146
	C(25)–H(25)···N(111)$^{\#3}$	0.95	2.60	3.52(5)	164
	C(55)–H(55)···N(101)$^{\#3}$	0.95	2.60	3.52(4)	163
	C(73)–H(73)···N(102)$^{\#3}$	0.95	2.60	3.28(4)	129
	C(83)–H(83)···N(93)$^{\#4}$	0.95	2.45	3.24(3)	141
	C(85)–H(85)···N(96)$^{\#5}$	0.95	2.58	3.42(3)	148

[a]Symmetry transformations used to generate equivalent atoms: #1 *x*, *y*, 1 + *z*; #2 –1 + *x*, *y*, *z*; #3 *x*, –1 + *y*, *z*; #4 2 – *x*, 1 – *y*, –*z*; #5 1 + *x*, *y*, *z*.

[b]Symmetry transformations used to generate equivalent atoms: #1 2 – *x*, –*y*, 2 – *z*; #2 1 – *x*, 1 – *y*, 2 – *z*; #3 1 + *x*, *y*, *z*; #4 –*x*, 1 – *y*, 1 – *z*; #5 1 – *x*, –*y*, 1 – *z*.

Table 3

π···π distances (Å) and angles (°) for **1** and **2**[a].

	Cg(*I*)	Cg(*J*)	*d*[Cg(*I*)–Cg(*J*)]	*α*	*β*	*γ*
1[b]	Cg(5)	Cg(5)$^{\#1}$	3.710(2)	0.00(19)	22.0	22.0
2[c]	Cg(3)	Cg(6)$^{\#1}$	3.758(16)	10	28.0	20.0
	Cg(6)	Cg(3)$^{\#2}$	3.759(16)	10	20.0	28.0
	Cg(9)	Cg(13)$^{\#2}$	3.979(13)	19	38.0	21.2
	Cg(13)	Cg(9)$^{\#1}$	3.979(13)	19	21.2	38.0

[a]Cg(*I*)–Cg(*J*): distance between ring centroids; *α*: dihedral angle between planes Cg(*I*) and Cg(*J*); *β*: angle Cg(*I*) → Cg(*J*) vector and normal to plane *I*; *γ*: angle Cg(*I*) → Cg(*J*) vector and normal to plane *J*.

[b]Symmetry transformations used to generate equivalent atoms: #1 2 – *x*, –*y*, –*z*. Cg(5): N(22)–C(23)–C(24)–C(25)–C(26)–C(27).

[c]Symmetry transformations used to generate equivalent atoms: #1 –1 + *x*, *y*, *z*; #2 1 + *x*, *y*, *z*. Cg(3): N(22)–C(23)–C(24)–C(25)–C(26)–C(27); Cg(6): C(34)–C(35)–C(36)–C(37)–C(38)–C(39); Cg(9): N(52)–C(53)–C(54)–C(55)–C(56)–C(57); Cg(13): C(64)–C(65)–C(66)–C(67)–C(68)–C(69).

Reaction of one or two equivalents of 5-phenyl-2,2'-bipyridine (**L**) with a mixture of one equivalent of $CoCl_2$ and two equivalents of NaN_3 leads to mononuclear heteroleptic cobalt(III) complexes $[CoL_2(N_3)_2](N_3)_{0.55}Cl_{0.45}\cdot EtOH$ (**1**) and $[CoL_2(N_3)_2]N_3\cdot 2.5EtOH$ (**2**), respectively. Both compounds are potential materials for the release of thermal energy. DFT calculations rationalize the stability of the synthesized materials.

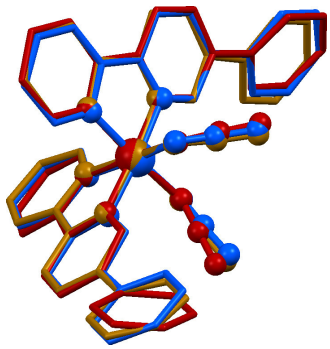

We synthesized mononuclear cobalt(III) complexes $[CoL_2(N_3)_2](N_3)_{0.55}Cl_{0.45}\cdot EtOH$ (**1**) and $[CoL_2(N_3)_2]N_3\cdot 2.5EtOH$ (**2**).

1 is stable up to 63 °C and decomposes in three steps, while **2** decomposes at 84 °C in two steps.

DFT calculations shed light on possible spin states and rationalize the stability of **1** and **2**.